Available online at www.sciencedirect.com
SCIENCE DIRECT®
Optics Communications 259 (2006) 265–273
OPTICS COMMUNICATIONS
www.elsevier.com/locate/optcom

Femtosecond filamentation in air at low pressures: Part I: Theory and numerical simulations

A. Couairon [a,*], M. Franco [b], G. Méchain [b], T. Olivier [b], B. Prade [b], A. Mysyrowicz [b]

[a] Centre de Physique Théorique, École Polytechnique, CNRS UMR 7644, F-91128, Palaiseau Cedex, France
[b] Laboratoire d'Optique Appliquée, École Nationale Supérieure des Techniques Avancées-École Polytechnique, CNRS UMR 7639, F-91761 Palaiseau Cedex, France

Received 10 March 2005; received in revised form 27 August 2005; accepted 30 August 2005

Abstract

We investigate numerically the influence of the pressure on femtosecond filamentation in air. We show that femtosecond filamentation occurs at low pressure and compute the features of the plasma channel generated in the wake of the pulse. We discuss the influence of the pulse duration, chirp and input beam shape on the length of the plasma channels. These calculations constitute a prerequisite for laboratory experiments over short distances as well as for vertical femtosecond filamentation at high altitude on which light detection and ranging techniques or lightning protection rely.

PACS: 42.25.Bs; 42.65.Jx; 42.65.Sf; 52.38.Hb

1. Introduction

The propagation in gases or in condensed media of femtosecond laser pulses with powers exceeding the critical power for self-focusing $P_{cr} \equiv 3.77\lambda^2/8\pi n_0 n_2$ (3 GW in air at $\lambda = 800$ nm) [1] generates specific structures called filaments [2–4]. A filament possesses a narrow central core (diameter of about 100 μm in air) surrounded by a laser energy reservoir [5]. Powerful beams usually form multiple filaments fed by this energy reservoir. Their global evolution involves a dynamical competition between several physical effects. Diffraction, Kerr self-focusing, photo-ionization, multiphoton absorption participate in the dynamics. The pulse temporal profile is also significantly modified due to group velocity dispersion, self-phase modulation and self-steepening.

Several applications rely on specific properties of femtosecond filaments. Three properties are particularly interesting: (i) Light filaments can propagate horizontally over distances exceeding 2 km [6–8] and vertically over distances presumably reaching several kilometers [9,10]. (ii) Light filaments produce, via self-phase modulation, a white light continuum [3,11,12]. For instance, light detection and ranging (LIDAR) techniques use both properties and allow the detection of pollutants in the atmosphere when the laser pulse is launched in the sky and the backscattered light is collected by a telescope and analyzed [13]. (iii) Light filaments produce ionized channels in their wake. The triggering and guiding of electric discharges by a filament has been demonstrated in the laboratory, over distances of several meters [14–18], see [19] for a review. These scales must be extended to hundreds of meters for practical applications.

Both for lightning protection and LIDAR applications, the pressure evolves from the atmospheric pressure to a few tenths of bars at an altitude of 10 km. It has been shown recently that a control of filamentation can be achieved over horizontal kilometric distances by varying the chirp of the input pulse [7,8]. In order to achieve a control of the filamentation process in the atmosphere, the properties

* Corresponding author. Tel.: +33 1 69 33 47 24; fax: +33 1 69 33 30 08.
E-mail address: couairon@cpht.polytechnique.fr (A. Couairon).

0030-4018/$ - see front matter © 2005 Elsevier B.V. All rights reserved.
doi:10.1016/j.optcom.2005.08.064

of filaments must be studied in detail as a function of the pressure.

The aim of the present paper is to present theoretical investigations on femtosecond filaments propagating in air at various pressures from 0.1 to 1 atm. This study shows the influence of various control parameters of the input pulse. Calculations are performed for pulse durations of 60 fs, 120 fs and 500 fs, with the longest durations obtained by chirping the shortest pulse. The influence of the shape of the input beam is also studied. This parameter is shown to play an important role in the physics of filamentation. In particular, the length of the plasma column generated in the wake of the pulse vary with the shape of the input beam and can be significantly enhanced by using diaphragmed input beams with steep intensity gradients. The general trends show the existence of low pressure filaments, as well as the increase in the length of the plasma channels at lower pressures. The simulations also show that a chirp in the input pulse allows the generation of a plasma channel from a nonlinear focus located at a larger distance without significant change in the channel length. Finally, the numerical results show that femtosecond filamentation can occur at low pressures ($0.2 \leqslant p \leqslant 1$ atm), which corresponds to altitudes higher than 10 km.

The outline of this paper is the following: First, we present the physical model in Section 2. In Section 3, we present numerical results about the propagation of laser pulses in air at low pressures and the generation of plasma channels. In Section 4, we present results showing the influence of the pulse duration. The influence of the beam focusing is studied in Section 5. The influence of the shape of the input beam is shown in Section 6. Finally, conclusions and outlook are given in Section 7.

2. Numerical simulations

The numerical code used in this study relies on the physical model developed for the propagation of an intense pulse in noble gases or air [7,8,20–23], fused silica [24–26], and liquids [27–29].

We model the linearly polarized beam with cylindrical symmetry around the propagation axis z by the envelope $\mathscr{E}$ of the electric field $\mathbf{E}$, written as $\mathbf{E} = \mathrm{Re}[\mathscr{E}\exp(\mathrm{i}kz - \mathrm{i}\omega_0 t)]$, where $k = n_0\omega_0/c$ and ω_0 are the wavenumber and frequency of the carrier wave and n_0 denotes the refraction index of air. In the following, these quantities correspond to a laser wavelength of 800 nm. The input pulses were modeled by Gaussians with energy E_{in} and a temporal FWHM duration τ_{FWHM} (temporal half width t_p):

$$\mathscr{E}(r,t,0) = \mathscr{E}_0 \exp\left(-\frac{r^n}{w_0^n} - \frac{t^2}{t_p^2} - \mathrm{i}\frac{kr^2}{2f} - \mathrm{i}C\frac{t^2}{t_p^2}\right). \tag{1}$$

The input power is computed from the energy and pulse duration $P_{\mathrm{in}} = E_{\mathrm{in}}/t_p\sqrt{\pi/2}$ and the input intensity is computed from the input power, the transverse waist w_0 and the shape of the beam. For a Gaussian beam ($n = 2$), $\mathscr{E}_0^2 = 2P_{\mathrm{in}}/\pi w_0^2$ whereas for a super-Gaussian beam $\mathscr{E}_0^2 = [P_{\mathrm{in}}/2\pi w_0^2] \times [n2^{2/n}/\Gamma(2/n)]$. The quantity f denotes the curvature of the input beam and C the chirp of the input pulse, linked to the minimum pulse duration (according to the laws of Gaussian optics) $t_p^{\min} = t_p/\sqrt{1+C^2}$ and the second order derivative $\phi^{(2)} = Ct_p^2/2(1+C^2)$.

We have performed various set of experiments using diaphragmed beams. In order to mimic input beams obtained in usual experiments on filamentation, the numerical simulation can start either with Gaussian or super-Gaussian beams. Their feet can also be masked by requiring $\mathscr{E}(r,t,z=0) = 0$ for $r > r_{\mathrm{mask}}$ so as to model a circular aperture.

Two coupled equations describe the evolution of the envelope of the electric field and the electron density. The scalar envelope $\mathscr{E}(r,t,z)$ is assumed to be slowly varying in time. It evolves along the propagation axis z according to the nonlinear envelope equation [30], expressed in the frequency domain:

$$\hat{U}\frac{\partial\hat{\mathscr{E}}}{\partial z} = \mathrm{i}\left[\frac{\nabla_\perp^2}{2k} + \frac{k}{2}\left(\frac{n^2\omega^2}{k^2c^2} - \hat{U}^2\right)\right]\hat{\mathscr{E}} + \mathrm{TF}\{N(\mathscr{E})\}, \tag{2}$$

where $\hat{\mathscr{E}}(r,\omega,z) = \mathrm{TF}\{\mathscr{E}(r,t,z)\}$, $\hat{U}(\omega) \equiv 1 + (\omega-\omega_0)/kv_{\mathrm{g}}$, $v_{\mathrm{g}} \equiv \partial\omega/\partial k|_{\omega_0}$ denotes the group velocity and $\mathrm{TF}\{N(\mathscr{E})\}$ denotes the time-Fourier transform of the nonlinear terms. Eq. (2) accounts for diffraction in the transverse plane, group velocity dispersion and high-order dispersive terms exactly computed by means of a Sellmeier dispersion relation for the refraction index $n(\omega)$ of air. The operator $\hat{U}$ in front of $\partial/\partial z$ in Eq. (2) accounts for space–time focusing (see [30,31]). A small $\omega - \omega_0$ expansion of the quantity

$$\hat{U}^{-1}\left(\frac{n^2\omega^2}{k^2c^2} - \hat{U}^2\right) \sim \frac{k''}{k}(\omega-\omega_0)^2 + \frac{k'''}{3k}(\omega-\omega_0)^3 + \cdots \tag{3}$$

leads to the second and third order dispersive coefficients $k'' \equiv \partial^2 k/\partial\omega^2|_{\omega_0} = 0.2$ fs^2/cm and $k''' \equiv \partial^3 k/\partial\omega^3|_{\omega_0} = 0.1$ fs^3/cm at 800 nm. Eq. (2) can be written in the time domain by using the retarded time $t \equiv t_{\mathrm{lab}} - z/v_{\mathrm{g}}$ and by neglecting the high-order dispersive terms:

$$\frac{\partial\mathscr{E}}{\partial z} = \left[\frac{\mathrm{i}}{2k}U^{-1}\nabla_\perp^2 - \mathrm{i}\frac{k''}{2}\frac{\partial^2}{\partial t^2} + \frac{k'''}{6}\frac{\partial^3}{\partial t^3}\right]\mathscr{E} + U^{-1}N(\mathscr{E}), \tag{4}$$

where $U \equiv (1 + \frac{\mathrm{i}}{kv_{\mathrm{g}}}\frac{\partial}{\partial t})$ and the nonlinear effects include the optical Kerr effect with a nonlocal term corresponding to delayed Raman–Kerr optical shock response [32,33], self-steepening, plasma absorption, plasma defocusing and multiphoton absorption:

$$N(\mathscr{E}) = \mathrm{i}k_0n_2T^2\left[(1-f_{\mathrm{R}})|\mathscr{E}(t)|^2 + f_{\mathrm{R}}\int_{-\infty}^{t}\mathrm{d}\tau R(\tau-t)|\mathscr{E}(\tau)|^2\right] \times \mathscr{E}(t) - \frac{\sigma}{2}(1+\mathrm{i}\omega_0\tau_{\mathrm{c}})\rho\mathscr{E} - T\frac{\beta_K}{2}\left(1-\frac{\rho}{\rho_{\mathrm{at}}}\right)|\mathscr{E}|^{2K-2}\mathscr{E}. \tag{5}$$

The operator $T \equiv 1 + \frac{i}{\omega_0}\frac{\partial}{\partial t}$ in front of the Kerr term is responsible for the self-steepening of the pulse [31,34,35]. Self-focusing related to the Kerr effect occurs for pulses with P_{in} above $P_{cr} = 3$ GW. This critical value corresponds to the nonlinear refraction index of air $n_2 = 3.2 \times 10^{-19}$ cm^2/W at $p = 1$ bar, which we used in our simulations. From [32,36], the response function that accounts for the delayed Raman contribution in the Kerr effect may be written as

$$R(t) = \Omega^2 \tau_s \exp\left(-\frac{t}{\tau_d}\right) \times \sin\left(\frac{t}{\tau_s}\right),$$

with the characteristic times $\tau_d = 70$ fs and $\tau_s = 63$ fs, $\Omega^2 = \tau_s^{-2} + \tau_d^{-2} = 21$ THz, and fraction $f_R = 0.5$.

For plasma absorption, the cross-section for inverse bremsstrahlung follows the Drude model [37] and reads

$$\sigma = \frac{ke^2}{n_0^2 \omega_0^2 \epsilon_0 m} \times \frac{\omega_0 \tau_c}{1 + \omega_0^2 \tau_c^2}, \tag{6}$$

where the momentum transfer collision time $\tau_c = 350$ fs at $p = 1$ bar. Since $\tau_c \gg \omega_0^{-1} = 0.42$ fs, the classical plasma defocusing term is retrieved in Eq. (5):

$$-i\frac{\sigma \omega_0 \tau_c \rho \mathscr{E}}{2} \sim -i\frac{k\rho}{2n_0^2 \rho_c}\mathscr{E},$$

where ρ_c denotes the critical plasma density above which the plasma becomes opaque.

The evolution equation for the electron density reads

$$\frac{\partial \rho}{\partial t} = \sigma_K |\mathscr{E}|^{2K}(\rho_{at} - \rho) + \frac{\sigma}{U_i}\rho|\mathscr{E}|^2. \tag{7}$$

The first term on the right-hand side of Eq. (7) describes free electron generation via multiphoton ionization of oxygen with neutral atom density $\rho_{at} = 0.2\rho_{air}$, involving $K \equiv \langle \frac{U_i}{\hbar\omega_0} + 1 \rangle$ photons. The quantity $U_i = 12.06$ eV denotes the ionization potential of oxygen molecules and $\langle \cdot \rangle$ denotes the integer part. At 800 nm, $K = 8$ photons are necessary and the photoionization rate of oxygen molecules is computed in the framework of Keldysh's general formulation [38] revisited by Mishima et al. [39] so as to take into account a specific preexponential factor for diatomic molecules. In the multiphoton ionization regime $W_{PI} = \sigma_K |\mathscr{E}|^{2K}$, where $\sigma_K = 3.7 \times 10^{-96}$ s^{-1} cm^{16} W^{-8}. The multiphoton absorption cross-section reads as $\beta_K = \sigma_K \times K\hbar\omega_0\rho_{at} = 3.7 \times 10^{-95}$ cm^{13} W^{-7}. The second term in Eq. (7) accounts for avalanche ionization.

Some of the parameters in this model vary with the pressure of the gas. The values given above corresponds to a gas of 1 atm and their variation with the pressure in the range 0.1–10 atm is as follows:

$$n_2 = n_{2,0} \times p, \quad \tau_c = \tau_{c,0}/p, \quad \sigma = \sigma_0 \times \frac{p(1 + \omega_0^2 \tau_{c,0}^2)}{p^2 + \omega_0^2 \tau_{c,0}^2},$$

$$\rho_{at} = \rho_{at,0} \times p, \quad \beta_K = \beta_{K,0} \times p,$$

where p is expressed in atm and the index 0 denotes atmospheric pressure at sea level. These expressions show that the nonlinear dynamics is not expected to be trivially rescaled with air pressure, which enters in the plasma induced defocusing and plasma absorption terms with a different power than in other nonlinear terms. Therefore, the numerical investigation is important in order to reveal the changes in the competition between the nonlinear effects when the pressure varies.

Our numerical code contains several numerical scheme as explained in [23]. One of the most efficient follows a standard split step Crank–Nicholson scheme applied to each frequency corresponding to the Fourier decomposition in time of the pulse. It is clearly a formidable computational task to propagate a pulsed beam over large distances due to the wide range of spatial and temporal scales involved. Adaptative unevenly distributed mesh grids allow us to adjust the resolution to this wide range going from the micron scale to a few centimeters and from a fraction of fs to ps durations [8]. Usually, a resolution of 5–10 μm in the transverse direction and 1–3 fs in the time direction is sufficient for most weakly nonlinear situations whereas much higher resolution is achieved around the peak intensities, with this adaptative mesh, when necessary. The gain in computational time corresponds to a factor of 10 when this standard Crank–Nicholson–Fourier scheme is used with an adaptative mesh, compared to the case of a mesh with constant step sizes.

3. Long distance propagation of collimated beams at low pressures

Laser pulses of 50 mJ energy and 120 fs duration (FWHM) are first shown to lead to filamentation over long distances when they propagate in air at low pressures from 0.2 to 1 atm. The restriction to cylindrical symmetry might seem questionable in the case of large peak input powers because a real beam is inherently non-homogeneous and undergoes beam-breakup and multiple filamentation. We investigate however the ideal case where a perfectly clean, and possibly powerful, input beam is launched and leads to a single filament. Among the reasons, there is the fact that our (3+1)D simulation code does not lead to a symmetry breaking when it is initiated by a pulsed cylindrically symmetric beam, without noise. The break-up of a powerful beam into multiple beamlets which eventually evolve into filaments actually depends on the level of input noise, as recently shown in [40]. The nonlinear saturation of the growing beamlets can also prevent the formation of a fully developed multifilamentation pattern as predicted by linear stability analyses [41,42]. In addition, a large number of (3+1)D simulations would be necessary to perform various statistical realizations and obtain a valuable information about the multiple filaments initiated with a white noise, which is beyond the scope of the present paper. We therefore describe the physics of a single filament in interaction with its surrounding energy reservoir. This is relevant even if the filament is produced by a pulse with high peak input power since several experimental situations show that

multiple filaments in air interact through their mutual energy reservoir [7,8,21,43].

Fig. 1 shows simulation results for the fluence, intensity, electron density and beam width obtained from a collimated Gaussian input beam with $n = 2$ and $w_0 = 14$ mm launched in air at three different pressures. Figs. 1(a1)–(a3) correspond to the lowest pressure of 0.2 bar. The fluence profile in Fig. 1(a1) shows a light filament exhibiting several peaks and radiation losses emitted from the core at each of these peaks. The filament starts at $z = 80$ m and propagates beyond 250 m. At low pressures between 0.6 and 1 bar, Figs. 1(b1) and (c1) also show evidence of an extended filamentation, with refocusing peaks located at distances larger than 300 m. The peak intensity and the peak electron density are plotted as functions of the propagation distance in Figs. 1(a2), (b2), (c2). They reach saturation at the levels 2×10^{13} W/cm^2 and 2–10×10^{15} cm^{-3}. The ratio of the saturation levels for the electron density obtained at different pressures follows the ratio of the gas pressures. This effect is due to intensity clamping as explained in Section 5. The nonlinear focus beyond which the plasma string is generated is located at smaller propagation distances when the pressure is increased. This effect is well explained by the fact that the critical power for self-focusing scales as $1/p$, and therefore decreases when the pressure increases. Thus, the location of the nonlinear focus decreases because it is closer to the laser when the effective ratio $P_{\rm in}^{\rm eff}/P_{\rm cr}$ is large. As shown in [44] the position of the nonlinear focus $z_{\rm nf}$ as a function of $P_{\rm in}^{\rm eff}/P_{\rm cr}$ follows a Marburger-like scaling law when a Raman contribution is present in the Kerr effect:

$$z_{\rm nf} = \frac{0.367 z_{\rm R}}{\sqrt{\left[\left(\max_t P_{\rm in}^{\rm eff}(t)/P_{\rm cr}\right)^{1/2} - 0.852\right]^2 - 0.0219}}, \tag{8}$$

where $z_{\rm R}$ denotes the Rayleigh length and

$$P_{\rm in}^{\rm eff}(t) = P_{\rm in}[(1 - f_{\rm R})\exp(-2t^2/t_p^2) + f_{\rm R}\int_{-\infty}^{t} R(t' - t) \times \exp(-2(t'/t_p)^2)\,{\rm d}t']. \tag{9}$$

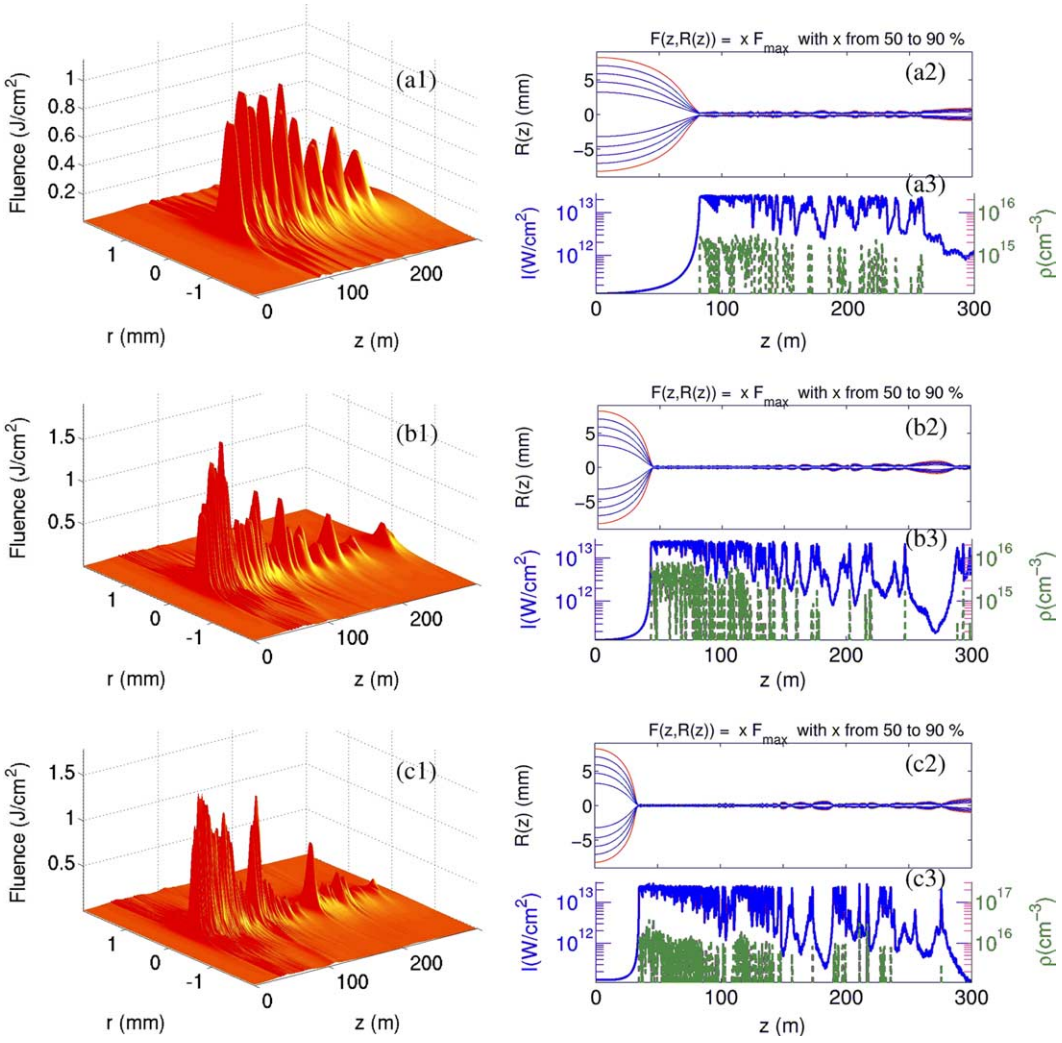

Fig. 1. Propagation of a 50 mJ, 120 fs laser pulse in the atmosphere at (a) 0.2 bar, (b) 0.6 bar and (c) 1 bar. The input beam is a collimated Gaussian with $w_0 = 14$ mm. (a1), (b1), (c1) Fluence profile as a function of the propagation distance. (a2), (b2), (c2) Intensity (continuous curve, left axis) and electron density (dashed curve, right axis) vs. z. (a3), (b3), (c3) Beam width vs. z. The levels correspond to a fraction of the maximum fluence, from 50% to 90%.

We have also performed numerical simulations (not shown) with a continuously decreasing pressure with altitude, so as to model a vertical propagation. In these simulations, p varies with the altitude according to the simple isothermal model (between 0 and 11 km): $p = p_0\exp(-(z - z_0)/z_p)$, where $z_p \equiv RT/Mg \simeq 8$ km. Since the typical filamentation scale of about 100 m is much smaller than z_p, no significant changes in the filament and plasma channels were obtained in comparison with the case of a constant low pressure. Filamentation occurs over several hundreds of meters in both cases with discontinuous plasma channels.

4. Influence of the chirp of the input pulse on the plasma channel

Another parameter playing a crucial role is duration of the input pulse. When experiments are performed with a single laser, the pulse duration is controlled by modifying the chirp of the input pulse. Usually, the propagation of ultrashort laser pulses over long distances is achieved by precompensation of the group velocity dispersion of air. This is done by means of a negative chirp in the initial pulse, which therefore becomes longer and consequently, contains less power. A theoretical analysis of the filamentation length with chirped pulses satisfying these conditions has been done in [45]. This analysis shows that the filamentation length is enhanced for large negative chirps, provided the dispersive-compression length (defined as the distance necessary to compress the chirped pulse owing to group velocity dispersion) slightly exceeds the self-focusing distance (defined by Eq. (8)). This result is in agreement with experimental results in [8]. Fig. 2 shows a comparison between the plasma channels generated by numerical simulation of the propagation of chirped and non chirped pulses (minimum duration of $t_p = 120$ fs), with either collimated or focused Gaussian input beams (focal length of $f = 50$ m), 50 mJ energy and $w_0 = 14$ mm. Fig. 2(a) corresponds to a non-chirped pulse and collimated beam: the nonlinear focus is located at a distance of 30 m from the source, which is comparable to the value $z_{nf} = 31$ m predicted by Eq. (8). The plasma channel generated on axis is not continuous but appears by bursts. Its total length, defined as the distance over which the on-axis electron density exceeds 10^{15} cm^{-3}, is about 69 m. The propagation of a pulse with the same parameters except for the chirp $\phi^{(2)} = -3\times10^4$ fs^2 (corresponding to an input duration of 500 fs) shows that the nonlinear focus is located at 75 m from the source and the generated plasma channel is still discontinuous with a total length of about 47 m (Fig. 2(b)). Here, the dispersive compression length is about 1.5 km, much larger than the self-focusing length. By using pulses with the same energy and minimum duration, a negative chirp therefore delays the beginning of filamentation as expected but the extension of the generated plasma channel is only slightly smaller in agreement with the analysis in [45]. It

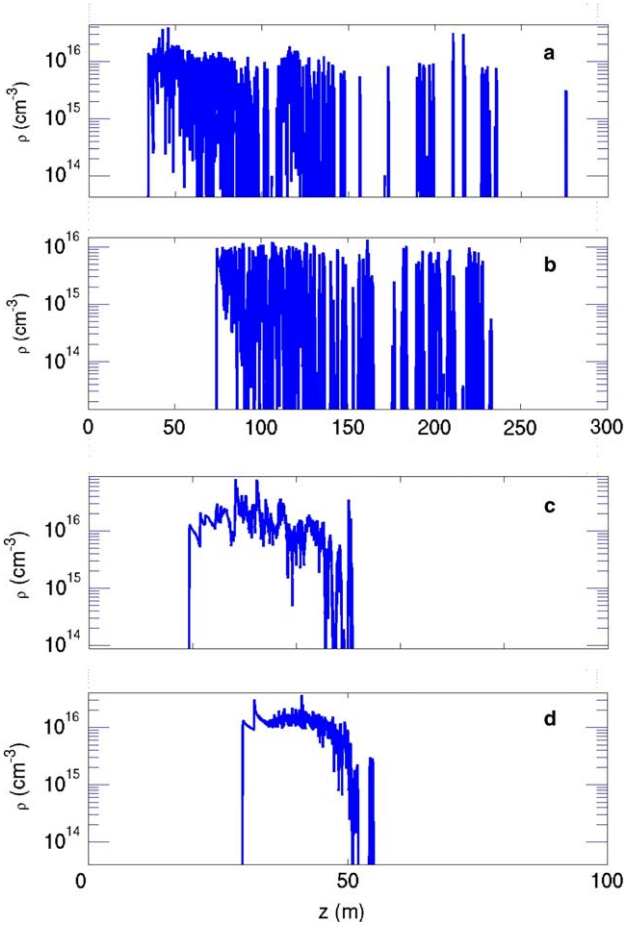

Fig. 2. Influence of the initial chirp on the plasma channel. (a) The input beam is Gaussian with $w_0 = 14$ mm, $E_{in} = 50$ mJ; the input pulse is not chirped with $t_p = 120$ fs. (b) Same conditions as in (a) with a chirp of -3×10^4 fs^2 (input pulse duration of 500 fs). (c) Same conditions as in (a) with a focused beam corresponding to a focal length $f = 50$ m. (d) Same conditions as in (c) with a chirp of -3×10^4 fs^2. Note that (a), (b) and (c), (d) have different scales for the propagation distance.

is worth noting that these simulations model single shot experiments. In an experiment, very close plasma bursts would be measured as a single continuous plasma channel, first because shot to shot fluctuations might lead to a natural averaging process and second because the measurement technique itself averages the electron density over a short centimetric scale.

5. Propagation of focused beams at low pressures

Figs. 2(c) and (d) show the electron density generated on-axis for the same pulses as in Section 4 except that the beam is now focused by a lens of focal length $f = 50$ m. The plasma channel generated with the unchirped pulse is now continuous. The focusing lens therefore facilitates the connection of the electron bursts into a single 28 m long channel, which starts closer to the laser. As in the case of the collimated beam, the chirped pulse associated with the focused beam generates a 21 m long continuous plasma channel but the beginning of the filament is

delayed (see Fig. 2(d)). The chirp of the input pulse therefore not only allows a shift of the beginning of filamentation but also a control of its length, whereas its continuity is controlled by the focal length. By tuning independently the focal length and the chirp, it is possible to produce various type of plasma channels. In practice, the choice of these parameters will depend whether a specific application needs a discontinuous plasma channels covering a large distance or a continuous plasma channel over a shorter range. In particular, a lens compresses the filamentation dynamics along the longitudinal direction. When a pulsed collimated beam generates the filament, it leads to successive focusing defocusing cycles reflecting the competition between the optical Kerr effect, multiphoton absorption and plasma induced defocusing. The periodicity between the pinching points of the beam, and

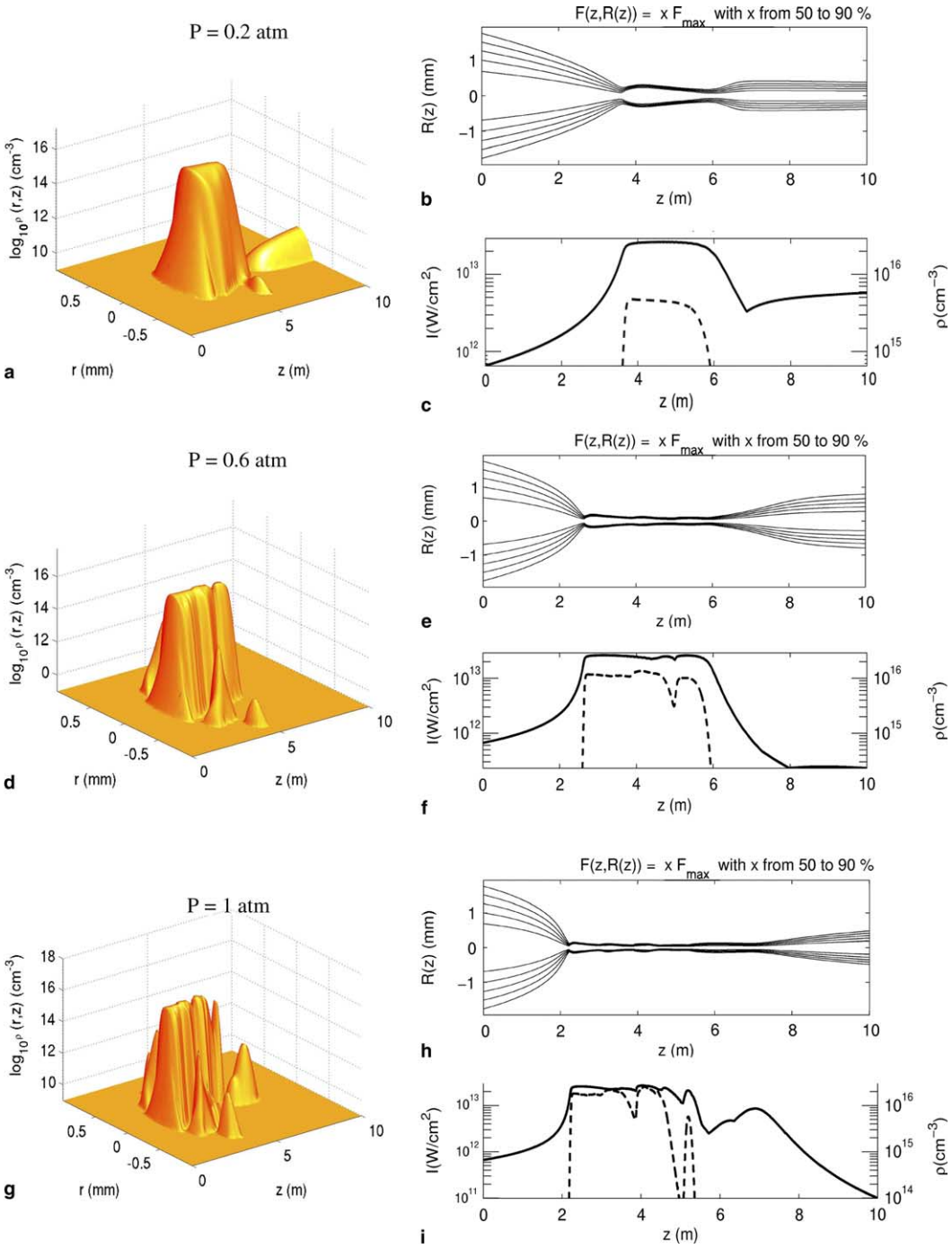

Fig. 3. Plasma channel generated in the wake of the ultrashort pulse for a Gaussian input beam with $w_0 = 3$ mm, $E_{in} = 6$ mJ, $f = 6$ m, $\tau_{FWHM} = 60$ fs. (a) $p = 0.2$ atm, (d) $p = 0.6$ atm and (g) $p = 1$ atm. (b) Beam diameter as a function of the propagation distance z for $p = 0.2$ atm. (e) and (h) same as in (b) for $p = 0.6$ and $p = 1$ atm. (c) Intensity (continuous line, left axis) and electron density (dashed line, right axis) vs. z for $p = 0.2$ atm. (f) and (i) same as in (c) for $p = 0.6$ and $p = 1$ atm.

thus the continuity of the plasma, depends on the input conditions. A pulsed beam with the same parameters, focused by a lens, will clearly produce a plasma channel with a shorter periodicity, located between the nonlinear focus and the position of the focus of the lens. If the focal length is sufficiently short, the plasma channel can become continuous. However, it is well known that it can also extend beyond the focus of the lens [46] with possible refocusing at larger distances.

It is therefore also interesting to study filamentation over laboratory scales since a prerequisite for experiments about long distance filamentation is to test the predictions of the calculations over shorter distances achievable in the laboratory. A forthcoming paper will describe laboratory experiments performed by using focal lengths in the meter range [47].

The following results corresponds to smaller energies and focused beams as used in laboratory experiments. Fig. 3 shows a comparison between the plasma channels numerically computed for $p = 0.2$, $p = 0.6$ and $p = 1$ atm. These results are obtained for a Gaussian input beam with $w_0 = 3$ mm, a focal length of 6 m and an input energy of 6 mJ. The pulse duration is $\tau_{\mathrm{FWHM}} = 60$ fs. Figs. 3(a), (d) and (g) show nearly connected plasma channels. The plasma strings undergo slight structural changes when the pressure is increased from 0.2 to 1 atm. The beam diameters shown in Figs. 3(b) (e) and (h) show that the nonlinear focus beyond which the filament starts is located farther on the propagation axis when the pressure is low. The maximum intensity shown in continuous line in Figs. 3(c), (f) and (i) slightly exceeds 10^{13} W/cm^2 but has comparable values in the three cases. The intensity clamping governed by a local balance between the index changes $n_2 I$ and $-\rho/2\rho_c$ is indeed insensitive to the pressure because both n_2 and ρ are proportional to the pressure. This result follows from the fact that the electron density is mainly given by its multiphoton contribution, in which case it scales as $\rho \simeq \sigma_K I^K \rho_{\mathrm{at}} t_p$. The maximum intensity therefore scales as $I \simeq (2n_2\rho_c/\sigma_K\rho_{\mathrm{at}}t_p)^{1/(K-1)}$ which does not depend on the pressure since $n_2/\rho_{\mathrm{at}} = n_{2,0}/\rho_{\mathrm{at},0}$, all other parameters being pressure independent. In contrast, the same scaling for the electron density shows that $\rho \propto p$. The maximum electron density shown in dashed curve on the same Figs. 3(c) and (i) is thus in the ratio 1/5 as it should be from the ratio of the pressures. The on-axis electron density increases with pressure. Computation at larger pressures ($p > 1$ atm) shows that the plasma channel becomes discontinuous (not shown).

The diameter of the ionized plasma channel is larger at lower pressure. As a result, integration of the electron density over the transverse dimension, i.e., the number of charges per centimeter exhibits only a smooth variation with pressure. Figs. 4(a)–(c) indeed show that the number of charges per cm which in principle is directly proportional to the electric conductivity of the plasma, reaches 10^{13} cm^{-1} for all pressures. The set of curves on each graph in Fig. 4 correspond to various integration radii (10, 50, 100 μm), the curve at the highest level reflecting the number of charges per cm in the whole beam.

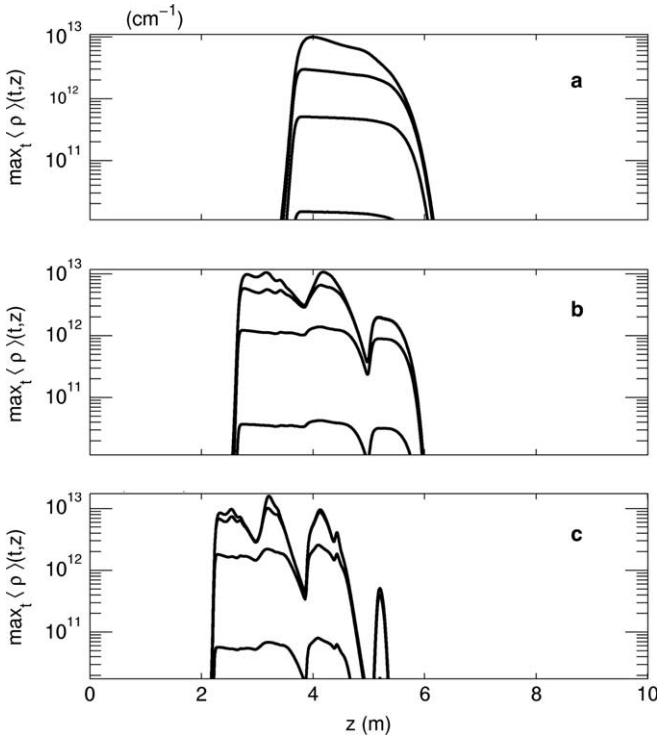

Fig. 4. Number of electrons per length unit as a function of the air pressure. The parameters are the same as in Fig. 3. (a) $p = 0.2$ atm, (b) $p = 0.6$ atm, (c) $p = 1$ atm. The curves on each graph correspond to different integration radii: 10, 50, 100 μm and the whole beam.

6. Influence of the input beam shape on the plasma column

Other input beam profiles have been used in the simulations. The general trends are recovered with all the beam profiles but some structural modifications of the plasma channels generated by the pulse occur. Fig. 5 shows the integrated electron density, i.e., the number of electrons per cm as a function of the propagation distance and the gas pressure for three different input beam profiles. The pulse has an energy of 5.4 mJ with a duration of 130 fs (FWHM). The focal length is $f = 2$ m. With a Gaussian input beam (see dotted curves in Fig. 5), the integrated electron density exhibits a 60 cm long main channel before the focus of the lens, reaching a few 10^{13} cm^{-1}. At 1 atm, two secondary plasma channels, nearly two orders of magnitude below the main channel, are formed further on the propagation axis (Fig. 5(a)). When the pressure decreases, the length of the principle plasma channel decreases. With a super-Gaussian input beam of order $n = 50$ (see continuous curves in Fig. 5), the main plasma channel is more spiky and a longer averaged plasma channel starting closer to the focus of the lens is obtained at an optimal pressure of 0.6 atm (Fig. 5(b)). With a diaphragmed Gaussian beam (dashed curves in Fig. 5), the same behavior is obtained except that the low level plasma channel extending beyond

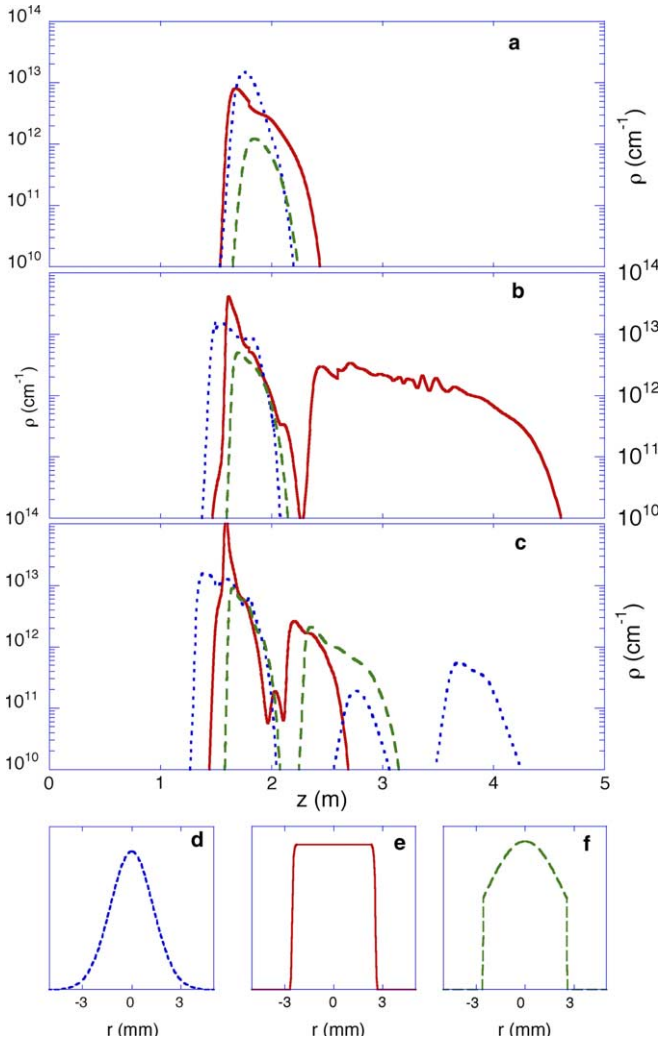

Fig. 5. Number of electrons per length unit as a function of the air pressure for various input beam profiles. The pulse parameters are $E_{in} = 5.4$ mJ, $t_p = 130$ fs, $f = 2$ m. (a) $p = 0.2$ atm, (b) $p = 0.6$ atm, (c) $p = 1$ atm. The different beam shapes are indicated by dotted, continuous, or dashed curves: dotted ≡ Gaussian input beam with $w_0 = 2.6$ mm (shown in (d)); continuous ≡ super-Gaussian input beam with $w_0 = 2.6$ mm and $n = 50$ (shown in (e)); dashed ≡ diaphragmed Gaussian input beam with $w_0 = 5.2$ mm and $r_{mask} = 2.6$ mm (shown in (f)).

the linear focus of the lens has a maximum length at a larger pressure than with a super-Gaussian input beam.

These results show that the shape of the input beam provides another sensitive control parameter for the length of the plasma channel.

7. Discussion and conclusion

The results show that femtosecond filamentation can occur at low pressures ($0.2 \leqslant p \leqslant 1$ atm), which corresponds to altitudes up to ~11 km. The effect of lowering the pressure modifies mainly the self-focusing stage during the propagation of the ultra-short pulse. The length of the plasma string does not change significantly in the range of pressure from 0.2 to 1 atm. Below 0.2 bar, the length is strongly reduced but this reflects the fact that the power is lower than the critical power for self-focusing. Indeed, the non-linear index of refraction n_2 related to the optical Kerr effect depends on the gaz density: $n_2 \propto p$. Therefore, as the critical power P_{cr} is inversely proportional to the non-linear index n_2, P_{cr} is inversely proportional to the gaz pressure. Hence, as the pressure decreases, the critical power increases and consequently the filament appears at a distance closer to the geometrical focus of the lens (or farther from the laser with collimated beams).

A second result concern the features of filamentation when the shape of the input beam vary. We have shown that this parameter, which is experimentally accessible, plays an important role in filamentation. For instance, it is possible to increase by a factor of two the length of the plasma channel generated in the wake of the ultrashort laser pulse, simply by introducing steep intensity gradients at the periphery of the input beam.

Finally, with a constant energy per pulse and a constant duration, the chirp of the input pulse has been shown to be of little influence on the length of the plasma channel generated by filamentation. However, if the input pulse is stretched by introducing a chirp, the power of the input beam is lowered and therefore, the beginning of filamentation is delayed in agreement with [7,8,45].

In conclusion, we have investigated by numerical simulations the influence of the pressure on filamentation. The calculations indicate the crucial influence of the shape of the input beam. In contrast, when the input pulse duration and power are constant, a chirp has little influence on filamentation. However, a chirp can be used as a control parameter to modify the duration of the input pulse and its power, which delays the beginning of filamentation and reduces the total length of the plasma channel. The plasma channel, however, may be discontinuous with bursts spread over a long distance. In a previous study [7,8], we have shown that large negative chirps allow an increase of the spread the plasma channels generated by horizontal propagation of ultrashort laser pulses at 1 atm. Finally, simulations of vertical filamentation with varying pressure have revealed filamentation over several hundreds of meters accompanied by disconnected plasma channels with a maximum electron density of 10^{16} cm^{-3}.

References

[1] J.H. Marburger, Prog. Quantum Electron. 4 (1975) 35.
[2] A. Braun, G. Korn, X. Liu, D. Du, J. Squier, G. Mourou, Opt. Lett. 20 (1995) 73.
[3] E.T.J. Nibbering, P.F. Curley, G. Grillon, B.S. Prade, M.A. Franco, F. Salin, A. Mysyrowicz, Opt. Lett. 21 (1996) 62.
[4] A. Brodeur, C.Y. Chien, F.A. Ilkov, S.L. Chin, O.G. Kosareva, V.P. Kandidov, Opt. Lett. 22 (1997) 304.
[5] M. Mlejnek, M. Kolesik, E.M. Wright, J.V. Moloney, Phys. Rev. Lett. 83 (1999) 2938.
[6] B.L. Fontaine, F. Vidal, Z. Jiang, C.Y. Chien, D. Comtois, A. Desparois, T.W. Johnston, J.-C. Kieffer, H. Pépin, Phys. Plasmas 6 (1999) 1615.

[7] G. Méchain, A. Couairon, Y.-B. André, C. D'Amico, M. Franco, B. Prade, S. Tzortzakis, A. Mysyrowicz, R. Sauerbrey, Appl. Phys. B 79 (2004) 379.
[8] G. Méchain, C. D'Amico, Y.-B. André, S. Tzortzakis, M. Franco, B. Prade, A. Mysyrowicz, A. Couairon, E. Salmon, R. Sauerbrey, Opt. Commun. 247 (2005) 171.
[9] L. Wöste, C. Wedekind, H. Wille, P. Rairoux, B. Stein, S. Nikolov, C. Werner, S. Niedermeier, F. Ronneberger, H. Schillinger, et al., Laser Optoelektron. 29 (1997) 51.
[10] M. Rodriguez, R. Bourayou, G. Méjean, J. Kasparian, J. Yu, E. Salmon, A. Scholz, B. Stecklum, J. Eislöffel, U. Laux, et al., Phys. Rev. E 69 (2004) 036607.
[11] J. Kasparian, R. Sauerbrey, D. Mondelain, S. Niedermeier, J. Yu, J.-P. Wolf, Y.-B. André, M. Franco, B. Prade, S. Tzortzakis, et al., Opt. Lett. 25 (2000) 1397.
[12] V.P. Kandidov, I.S. Golubtsov, O.G. Kosareva, Quantum Electron. 34 (2004) 348.
[13] P. Rairoux, H. Schillinger, S. Neirdeimer, M. Rodriguez, F. Ronneberger, R. Sauerbrey, B. Stein, D. Waite, C. Wedekind, H. Wille, et al., Appl. Phys. B 71 (2000) 573.
[14] D. Comtois, C.Y. Chien, A. Desparois, F. Génin, G. Jarry, T.W. Johnston, J.-C. Kieffer, B.L. Fontaine, F. Martin, R. Mawassi, et al., J. Appl. Phys. 76 (2000) 819.
[15] B.L. Fontaine, D. Comtois, C.Y. Chien, A. Desparois, F. Génin, G. Jarry, T.W. Johnston, J.-C. Kieffer, F. Martin, R. Mawassi, et al., J. Appl. Phys. 88 (2000) 610.
[16] P. Rambo, J. Schwarz, J.-C. Diels, J. Opt. A 3 (2001) 146.
[17] S. Tzortzakis, B. Prade, M. Franco, A. Mysyrowicz, S. Hüller, P. Mora, Phys. Rev. E 64 (2001) 057401.
[18] M. Rodriguez, R. Sauerbrey, H. Wille, L. Wöste, T. Fujii, Y.-B. André, A. Mysyrowicz, L. Klingbeil, K. Rethmeier, W. Kalkner, et al., Opt. Lett. 27 (2002) 772.
[19] N. Khan, N. Mariun, I. Aris, J. Yeak, New J. Phys. 4 (2002) 61.1.
[20] M. Mlejnek, E.M. Wright, J.V. Moloney, Opt. Lett. 23 (1998) 382.
[21] G. Méchain, A. Couairon, M. Franco, B. Prade, A. Mysyrowicz, Phys. Rev. Lett. 93 (2004) 035003.
[22] A. Couairon, G. Méchain, S. Tzortzakis, M. Franco, B. Lamouroux, B. Prade, A. Mysyrowicz, Opt. Commun. 225 (2003) 177.
[23] A. Couairon, S. Tzortzakis, L. Bergé, M. Franco, B. Prade, A. Mysyrowicz, J. Opt. Soc. Am. B 19 (2002) 1117.
[24] S. Tzortzakis, M. Franco, B. Prade, A. Mysyrowicz, A. Couairon, L. Bergé, Phys. Rev. Lett. 87 (2001) 213902.
[25] L. Sudrie, A. Couairon, M. Franco, B. Lamouroux, B. Prade, S. Tzortzakis, A. Mysyrowicz, Phys. Rev. Lett. 89 (2002) 186601.
[26] A. Couairon, L. Sudrie, M. Franco, B. Prade, A. Mysyrowicz, Phys. Rev. B 71 (2005) 125435.
[27] Q. Feng, J.V. Moloney, A.C. Newell, E.M. Wright, K. Cook, P.K. Kennedy, D.X. Hammer, B.A. Rockwell, C.R. Thompson, IEEE J. Quantum Electron. 33 (1997) 127.
[28] M. Kolesik, E.M. Wright, J.V. Moloney, Phys. Rev. Lett. 92 (2004) 253901.
[29] A. Dubietis, E. Gaižauskas, G. Tamošauskas, P.D. Trapani, Phys. Rev. Lett. 92 (2004) 253903.
[30] T. Brabec, F. Krausz, Phys. Rev. Lett. 78 (1997) 3282.
[31] A.L. Gaeta, Phys. Rev. Lett. 84 (2000) 3582.
[32] R.H. Stolen, J.P. Gordon, W.J. Tomlison, H.A. Haus, J. Opt. Soc. Am. B 6 (1989) 1159.
[33] G.K.L. Wong, Y.R. Shen, Phys. Rev. A 10 (1974) 1277.
[34] A.A. Zozulya, S.A. Diddams, T.S. Clement, Phys. Rev. A 58 (1998) 3303.
[35] A.A. Zozulya, S.A. Diddams, A.G.V. Engen, T.S. Clement, Phys. Rev. Lett. 82 (1999) 1430.
[36] J.-F. Ripoche, G. Grillon, B. Prade, M. Franco, E. Nibbering, R. Lange, A. Mysyrowicz, Opt. Commun. 135 (1997) 310.
[37] E. Yablonovitch, N. Bloembergen, Phys. Rev. Lett. 29 (1972) 907.
[38] L.V. Keldysh, Sov. Phys. JETP 20 (1965) 1307.
[39] K. Mishima, M. Hayashi, J. Yi, S.H. Lin, H.L. Selzle, E.W. Schlag, Phys. Rev. A 66 (2002) 033401.
[40] G. Fibich, Ê. Eisenmann, B. Ilan, Y. Erlich, M. Fraenkel, Z. Henis, A.L. Gaeta, A. Zigler, Opt. Exp. 13 (2005) 5897.
[41] A.J. Campillo, S.L. Chapiro, B.R. Suydam, Appl. Phys. Lett. 23 (1973) 628.
[42] A.J. Campillo, S.L. Chapiro, B.R. Suydam, Appl. Phys. Lett. 24 (1973) 178.
[43] W. Liu, J.-F. Gravel, F. Théberge, A. Becker, S.L. Chin, Appl. Phys. B 80 (2005) 857.
[44] A. Couairon, Eur. Phys. J. D 27 (2003) 159.
[45] I.S. Golubtsov, V.P. Kandidov, O.G. Kosareva, Quantum Electron. 33 (2003) 525.
[46] H.R. Lange, G. Grillon, J.-F. Ripoche, M.A. Franco, B. Lamouroux, B.S. Prade, A. Mysyrowicz, E.T.J. Nibbering, A. Chiron, Opt. Lett. 23 (1998) 120.
[47] G. Méchain, T. Olivier, M. Franco, A. Couairon, B. Prade, A. Mysyrowicz, Opt. Commun. (submitted).